Supporting Information

Frisz et al. 10.1073/pnas.1216585110

SI Materials and Methods

Analysis of Rare Isotope Incorporation. Cells were washed with PBS, detached, and collected via centrifugation, and the lipids were extracted (1). Separation and mass spectrometry were performed on an Agilent 1100 LC and an Agilent MSD Trap XCT Plus mass spectrometer. Incorporation of nitrogen-15 and ^{13}C-fatty acids into *N*-palmitoyl sphingomyelin was determined using positive ion peaks (Fig. S1). Contributions of isotopologues other than ^{15}N-palmitoyl sphingomyelin to *m/z* 704.6 were removed by subtracting 43.3% of the ^{14}N-palmitoyl sphingomyelin peak (*m/z* 703.6) intensity from peak *m/z* 704.6. Contributions of isotopologues other than ^{15}N-palmitoyl-$^{13}C_{16}$ sphingomyelin to *m/z* 720.6 were removed by subtracting 25.8% of the ^{14}N-palmitoyl-$^{13}C_{16}$ sphingomyelin peak (*m/z* 719.6) intensity from peak *m/z* 720.6. The incorporation of uniformly ^{13}C-labeled fatty acids was assessed as previously reported (2).

Analysis of ^{15}N-Enrichment in Phosphatidylethanolamine from Degradation of ^{15}N-Sphingomyelin. Lipids were extracted from cells labeled with ^{15}N-sphingolipid precursors for 24 d, which is four times longer than that for the cells analyzed by nano-secondary ion mass spectrometry (NanoSIMS). Phosphatidylethanolamine was isolated by preparative TLC (65:25:4 vol/vol/vol chloroform/methanol/water). Analysis of the extracted phosphatidylethanolamine on an automated N/C analyzer–mass spectrometer indicated <2% of ^{15}N-abundance (natural abundance = 0.37%).

Formation of Thin Iridium Layer on Cell Samples. To prevent charging during NanoSIMS analysis, a Cressington 208HR High-Resolution Sputter Coater equipped with a low-voltage planar magnetron sputter head, a rotary-planetary-tilting stage, and a Cressington MTM-20 High-Resolution Thickness Controller was used to produce the 3-nm-thick iridium coatings on the cells. The sample stage was rotated and tilted approximately ±30° during the entire metal sputtering process to minimize variations in the iridium coating thickness that might be caused by sample topography. To reduce the amount of impurities present in the resulting iridium metal coating on the samples, high-purity (99.95%) iridium was used as the source, and the source was presputtered to remove surface contamination before opening the shutter.

Calculation of Analysis Depth. Using Eq. **S1**, a sputtering rate of 2.5 nm·μm^{-2}·pA·s^{-1} determined on other biological samples (3), a total sputter time of 1,049 s, and a primary ion beam current of 0.129 pA, the sputtering depth for our analysis was 1.5 nm:

$$\text{Analysis depth} = \frac{\text{sputter rate} \times \text{primary ion beam current} \times \text{sputter time}}{\text{raster area}}. \quad \textbf{[S1]}$$

Quantitation of ^{15}N-Sphingolipid Domains. Statistically significant elevations in ^{15}N-enrichment that signify sphingolipid domains were outlined with a particle definition algorithm within a custom software package (L'image; L. R. Nittler, Carnegie Institution of Washington, Washington, DC) run with PV-Wave (Visual Numerics). This algorithm defined the domain centers as the pixels where the ^{15}N-enrichment factor was at a local maximum and at least 2 SD above the mean ^{15}N-enrichment factor for the nondomain membrane regions (4). The domain edges were located by expanding out from the center until the ^{15}N-isotope ratio dropped below the Gaussian diameter, which is 13.5% ($1/e^2$) of the ^{15}N-enrichment factor at the domain center, or until another domain was encountered (4).

Analysis of Sphingolipid Domain Organization. The clustering of the domains on the cell body was assessed using the SpatStat spatial statistics package (version 1.22-1) run in the R program (version 2.12.2) (5, 6). The *x–y* coordinates for the cell body were recorded by loading the montage of secondary electron images of the cell into GraphClick 3.0 and tracing the edges of the cell body but omitting the lamellipodia. The coordinates for the cell body were expressed in pixel units and were used to define the observation window in SpatStat. The *x–y* coordinates of the domain centers with respect to the whole cell were calculated from the coordinates of the pixels where the domain centers were located within each ^{15}N-enrichment image (exported from L'image) and the coordinates of each ^{15}N-enrichment image in the montage of the whole cell. These coordinates were used to create a point pattern that represented the observed domains within the observation window that corresponded to the cell body.

Ripley's K-test was performed on the point pattern corresponding to the domain centers, using translation edge correction to calculate the number of domains within a radius, r, of any domain on the cell surface (7, 8). Analysis was restricted to distances less than one-quarter of the smallest length of the observation window. Data were normalized to the 99% confidence interval, calculated according to

$$CI_{99} = 1.68\sqrt{A}/N.$$

A is the area of the observation window and N is the total number of domains within the window.

For comparison with the experimental domains observed on the cell surface, we simulated a population of spatially random domains within the observation window that represented the cell body. The number and effective diameters of the domains in the simulated population were identical to those that were experimentally observed on the cell body. We first determined the frequency distribution of effective domain diameters experimentally observed on the cell body, using a bin size of 1 pixel. We tabulated the number of domains with a specified effective diameter that were experimentally observed on the cell body. An algorithm was used to randomly add domains ("points") with the specified effective diameter (encoded as a "mark") one-by-one to the observation window that represented the cell body. New domains were generated independent of the preceding domains, and those that lay outside of the observation window were rejected. To prevent the domains from overlapping, the simulated domains were also rejected if the distance between the center of the simulated domain and the center of the closest domain was less than the sum of the radii of the two domains. Once the number of domains with a given diameter in the observation window equaled that experimentally observed on the cell body, the process was repeated for the next effective domain diameter. These steps were repeated until the correct number of domains had been simulated for every observed effective diameter.

The nearest neighbor distance, which is the distance from the center of each domain to the center of its nearest neighbor, was computed for each of the (*i*) experimentally observed domains on the cell body and (*ii*) simulated, spatially random domains. For each population (e.g., experimental and simulated), the frequency distribution of nearest neighbor domain distances was

tabulated using a bin size of 50 nm and normalized to the total number of domains in the population to produce the fraction of the total. The difference between the frequencies of observed and simulated nearest neighbor distances was calculated by subtracting the fraction of the simulated domain population with nearest neighbor distances within each 50-nm increment from the fraction of experimentally observed domains with nearest neighbor distances in the same range. The differences between the frequencies of observed and simulated nearest neighbor distances are plotted in Fig. 5*F*.

The pairwise domain distances, which are the distances between the center of each domain and the center of every other domain on the cell body, were computed for (*i*) every domain that was experimentally observed and (*ii*) every domain within the simulated population. The frequency distributions of pairwise domain distances for the experimental and simulated domains on each cell were tabulated using a bin size of 0.5 μm and normalized to the total number of domains in the population. The difference between the frequencies of observed and simulated pairwise domain distances was calculated for each 0.5-μm increment and is plotted in Fig. 5*G*.

Generation of Fluorescently Labeled Fab Fragments. Fab fragments of antihemagglutinin (anti-HA) antibody were generated using the ImmunoPure Fab Preparation Kit (Pierce), following the manufacturer's instructions. Briefly, anti-HA antibody (Covance) was subjected to papain digestion for 5 h at 37 °C. Fab fragments were subsequently purified by binding undigested antibody and Fc fragments to a Protein-A column. Collected fractions were pooled, concentrated, and dialyzed against PBS (pH 7.2, 12.5 mM Na_2HPO_4, 154 mM NaCl) containing 0.1% BSA. The concentrations of final solutions were determined by absorbance at 280 nm. Purified Fab fragments of anti-HA antibody were conjugated with Cy5.5, using the FastLink Cy5.5 Labeling Kit (Abnova) according to the manufacturer's protocol.

SI Control Experiments

Test for Analysis Artifacts Related to Sample Preparation and Topography. Unlabeled cells were cultured on lysine-coated silicon substrates and chemically fixed as described. Substrates with unlabeled cells as well as substrates with metabolically labeled cells were placed in the Cressington 208HR High-Resolution Sputter Coater and coated with a 3-nm-thick iridium layer as described above. NanoSIMS analysis of the unlabeled cells was performed with the same conditions used to analyze metabolically labeled cells. The secondary electron images acquired with NanoSIMS show the morphology and surface texture of the unlabeled cell (Fig. S2*A*). The ^{15}N- (Fig. S2*B*) and ^{13}C-enrichment (Fig. S2*C*) images show a uniform isotope composition equal to natural abundance was detected on the sample, independent of sample topography. Quantitative analysis of the 42,021 3 × 3-pixel subregions on the unlabeled Clone 15 cell confirmed no isotopic enrichment (enrichment factor equaling unity) was detected (mean ^{15}N-enrichment factor = 0.8, 1 SD = 0.6; mean ^{13}C-enrichment factor = 1.0, 1 SD = 4.4) on the cell. The absence of isotope enrichment and the lack of features in the isotope enrichment images demonstrate that sample topography does not significantly affect instrument alignment and the measured isotope enrichment factors.

Test for Artifacts Due to the Iridium Metal Coating. We comprehensively assessed the following four hypothetical mechanisms for artifactually creating ^{15}N-enriched domains on the cell surface: (*i*) disproportionate changes in the detection sensitivity of $^{12}C^{15}N^-$ and $^{12}C^{14}N^-$ and therefore giving the appearance of ^{15}N-enrichment; (*ii*) redistribution of the ^{15}N-sphingolipids on the cell surface; (*iii*) altering the amount of unlabeled (natural abundance) cytoplasmic material and thus the ratio of isotope-labeled cell membrane to natural abundance biomolecules, within the NanoSIMS analysis volume; and (*iv*) the presence of substantial amounts of natural abundance nitrogen-containing contamination in the iridium layer, causing the amount of $^{12}C^{14}N^-$ detected at each pixel to depend on the thickness of the iridium layer. These hypothetical mechanisms would putatively be related to lateral variations in the thickness or composition of the iridium metal coating. The uniform natural abundance isotopic ratios measured on the unlabeled (natural abundance) cell (Fig. S2, see *SI Methods* for details) exclude the possibility that the iridium coating disproportionally affected the collection of $^{12}C^{15}N^-$ and $^{12}C^{14}N^-$ and therefore the ^{15}N-enrichment (hypothetical mechanism *i*), as well as the possibility that the ^{15}N-sphingolipids were transferred to different samples during sputter coating. These results and prior reports that show the conductive metal coatings used for SIMS analysis do not redistribute the lipids on the cell surfaces (9) exclude the possibility that sputter coating redistributed the ^{15}N-sphingolipids on the cell surface (hypothetical mechanism *ii*).

In the third hypothetical mechanism, the ratio of isotope-labeled cell membrane components to unlabeled biomolecules in the underlying cytoplasm present within the NanoSIMS analysis volume varies as a function of the thickness of the iridium coating. We used a sputtering depth (<2 nm) that was much smaller than the thickness of the plasma membrane (7.5 nm) (10) to minimize the detection of significant numbers of secondary ions produced by cytoplasmic biomolecules. Analysis of the 3D isotope distribution in identically labeled cells confirmed that the elevated ^{13}C-enrichment was specific to the cellular lipids, and the ^{13}C-enrichment was not uniformly elevated throughout the cytoplasm, so iridium thickness-induced lateral variations in the amount of unlabeled cytoplasmic material within the NanoSIMS analysis volume would cause the ^{15}N- and ^{13}C-enrichment to vary in a correlated manner. The absence of statistically significant elevations in the ^{13}C-enrichment at the ^{15}N-enriched domains excludes the possibility that lateral variations in the iridium coating thickness induce significant lateral variations in the ratio of isotope-labeled cell membrane to natural abundance cytoplasmic biomolecules within the NanoSIMS analysis volume. Therefore, ^{15}N-enriched domains we detected in the plasma membrane with NanoSIMS cannot be attributed to hypothetical mechanism *iii*.

In the fourth hypothetical mechanism, the presence of natural abundance nitrogen-containing contamination in the iridium coating causes the amount of $^{12}C^{14}N^-$ detected at each pixel to vary as a function of the iridium coating thickness. Natural abundance nitrogen-containing contamination in the iridium coating could cause the number of $^{12}C^{14}N^-$ secondary ions to increase with increasing iridium coating thickness and thus the ^{15}N-enrichment ($[^{12}C^{15}N^-/^{12}C^{14}N^-]/0.00367$) to decrease with increasing iridium thickness. Such an iridium coating-thickness variation in $^{12}C^{14}N^-$ ion counts would affect any isotope enrichment that was calculated by ratioing to the $^{12}C^{14}N^-$ counts, including the ^{13}C-enrichment calculated by ratioing the carbon-13–containing cyanide ion to the naturally abundant cyanide ion ($[^{13}C^{14}N^-/^{12}C^{14}N^-]/0.011237$). Therefore, we assessed whether the lateral distribution of the ^{13}C-enrichment calculated using the CN isotopologues ($[^{13}C^{14}N^-/^{12}C^{14}N^-]/0.011237$) reflected the distribution of ^{15}N-enrichment on the cell surface or whether it accurately reflected the distribution of ^{13}C-enrichment that was calculated using the CH isotopologues ($[^{13}C^1H^-/^{12}C^1H^-]/0.011237$). NanoSIMS was used to collect the $^{12}C^1H^-$, $^{13}C^1H^-$, $^{12}C^{14}N^-$, $^{13}C^{14}N^-$, and $^{12}C^{15}N^-$ secondary ions from metabolically labeled cells. Secondary electron images were also acquired to permit correlating the isotope enrichment pattern with location on the cell (Fig. S4*A*). We constructed (*i*) ^{15}N-enrichment images using the ratio of the ^{15}N-enriched ion signal detected at each pixel to the abundant cyanide ion (i.e., $^{12}C^{15}N^-/^{12}C^{14}N^-$) (Fig. S4*B*), (*ii*) ^{13}C-enrichment images using the ratio of the ^{13}C-enriched CH ion signal detected at each pixel to the abundant CH ion ($^{13}C^1H^-/^{12}C^1H^-$) (Fig. S4*C*),

and (*iii*) ^{13}C-enrichment images using the ratio of the ^{13}C-enriched cyanide ion signal detected at each pixel to the abundant cyanide ion ($^{13}C^{14}N^-/^{12}C^{14}N^-$) (Fig. S4*D*). We then assessed whether the pattern of localized enrichment shown in the ^{13}C-enrichment image constructed using the $^{13}C^{14}N^-/^{12}C^{14}N^-$ ratio reflected the enrichment pattern visible in the ^{15}N-enrichment image or whether it accurately reproduced the pattern of enrichment shown in the ^{13}C-enrichment image that was constructed using the $^{13}C^1H^-/^{12}C^1H^-$ ratio. Local elevations in isotope enrichment were present in all three isotope enrichment images, including the ^{13}C-enrichment image calculated using the $^{13}C^1H^-/^{12}C^1H^-$ ratio, which confirms that artifactual elevations in the local abundance of cellular lipids can be detected in the ^{13}C-enrichment image. The ^{13}C-enriched domains visible in the ^{13}C-enrichment image constructed using the $^{13}C^{14}N^-/^{12}C^{14}N^-$ ratio (Fig. S4*D*) were at the same cellular locations as the domains visible in the ^{13}C-enrichment image constructed using the $^{13}C^1H^-/^{12}C^1H^-$ ratio (Fig. S4*C*). In contrast, the ^{13}C-enriched domains visible in the ^{13}C-enrichment image constructed using the $^{13}C^{14}N^-/^{12}C^{14}N^-$ ratio (Fig. S4*D*) were not at the same positions on the cell as the ^{15}N-enriched domains (Fig. S4*B*). This confirms that nitrogen-containing contamination in the iridium coating did not cause the amount of $^{12}C^{14}N^-$ detected at each pixel to vary as a function of the iridium coating thickness or cause the appearance of artifactual ^{15}N-enriched domains on the cell surface.

In conclusion, these control experiments and previous literature reports exclude the hypothetical mechanisms by which lateral variations in the thickness of the iridium coating might artifactually cause the appearance of ^{15}N-enriched domains in the plasma membrane.

1. Bligh EG, Dyer WJ (1959) A rapid method of total lipid extraction and purification. *Can J Biochem Physiol* 37(8):911–917.
2. Wilson RL, et al. (2012) Fluorinated colloidal gold immunolabels for imaging select proteins in parallel with lipids using high-resolution secondary ion mass spectrometry. *Bioconjug Chem* 23(3):450–460.
3. Ghosal S, et al. (2008) Imaging and 3D elemental characterization of intact bacterial spores by high-resolution secondary ion mass spectrometry. *Anal Chem* 80(15): 5986–5992.
4. Nittler LR (1996) Quantitative isotopic ratio ion imaging and its application to studies of preserved stardust in meteorites. PhD thesis (Washington University, St. Louis).
5. R Development Core Team (2010) *R: A Language and Environment for Statistical Computing* (R Foundation for Statistical Computing, Vienna).
6. Baddeley A, Turner R (2005) spatstat: An R package for analyzing spatial point patterns. *J Stat Softw* 12(6):1–42.
7. Prior IA, Muncke C, Parton RG, Hancock JF (2003) Direct visualization of Ras proteins in spatially distinct cell surface microdomains. *J Cell Biol* 160(2):165–170.
8. Dixon PM (2002) Ripley's K function. *Encyclopedia of Environmetrics*, eds El-Shaarawi AH, Piegorsch WW (Wiley, Chichester, UK), pp 1796–1803.
9. Altelaar AFM, et al. (2006) Gold-enhanced biomolecular surface imaging of cells and tissue by SIMS and MALDI mass spectrometry. *Anal Chem* 78(3):734–742.
10. Edidin M (2003) Lipids on the frontier: A century of cell-membrane bilayers. *Nat Rev Mol Cell Biol* 4(5):414–418.

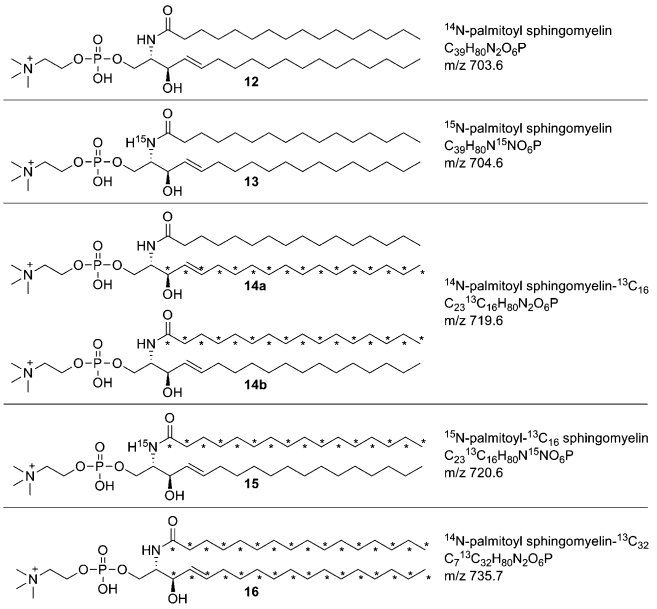

Fig. S1. Structures of cellular sphingomyelin isotopologues detected in cells cultured with exogenous ^{15}N-sphinganine and ^{15}N-sphingosine and UL-^{13}C-fatty acids. Exogenous UL-^{13}C-palmitic acid was biosynthetically incorporated into sphingomyelin at two metabolic steps: acylation of the sphingoid base (**14b**, **15**, and **16**); and de novo sphinganine biosynthesis (**14a** and **16**). Asterisks indicate ^{13}C-isotopes. For the cells that were metabolically labeled in the same culture as those analyzed with NanoSIMS, ^{15}N-sphingolipid precursors were incorporated into 83% of the *N*-palmitoyl sphingomyelin, and UL-^{13}C-palmitic acid was incorporated into 83% of the *N*-palmitoyl sphingomyelin. The fractions of *N*-palmitoyl sphingomyelin isotopologues **12**, **13**, **14** (**14a** and **14b**), **15**, and **16** in the cells were 0.05, 0.12, 0.07, 0.71, and 0.05, respectively. The fraction of ^{15}N-labeled *N*-palmitoyl sphingomyelin is the ratio of the sum of ^{15}N-palmitoyl sphingomyelin and ^{15}N-palmitoyl-$^{13}C_{16}$ sphingomyelin to the sum of all *N*-palmitoyl sphingomyelin isotopologues. The fraction of *N*-palmitoyl sphingomyelin biosynthesized from UL-^{13}C-palmitic acid is the ratio of the sum of ^{14}N-palmitoyl sphingomyelin-$^{13}C_{16}$, ^{15}N-palmitoyl sphingomyelin-$^{13}C_{16}$, and ^{14}N-palmitoyl sphingomyelin-$^{13}C_{32}$, over the sum of all *N*-palmitoyl sphingomyelin isotopologues.

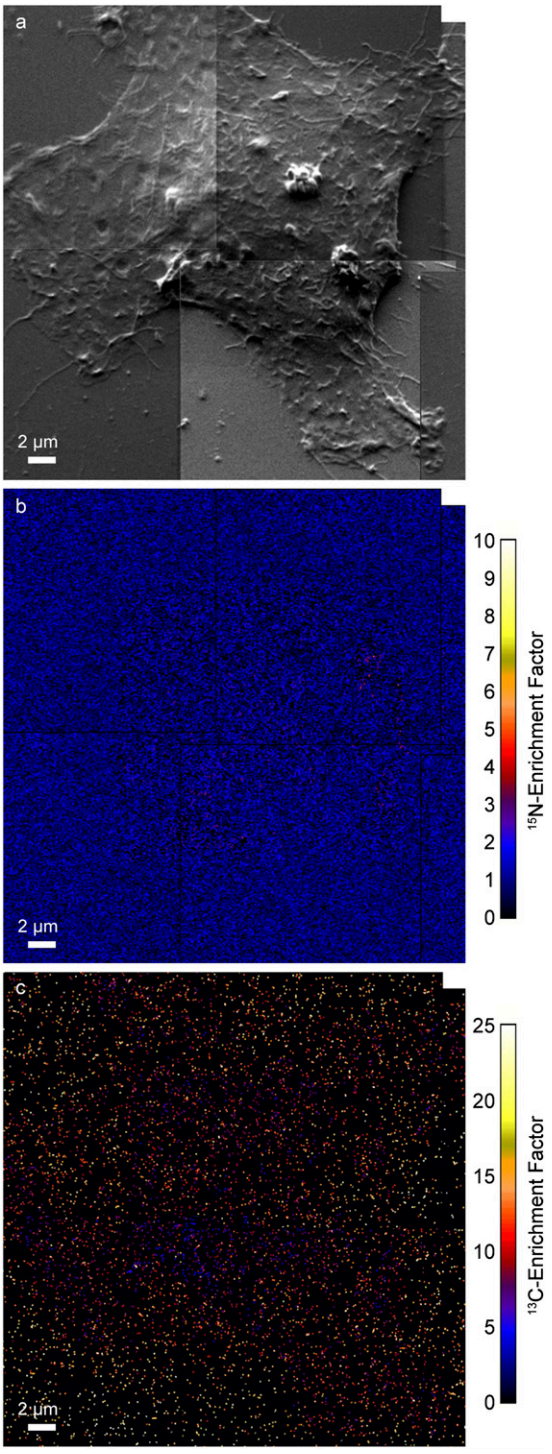

Fig. S2. NanoSIMS images of a representative unlabeled cell. Unlabeled (natural abundance) cells were analyzed with NanoSIMS to test for correct alignment, detector calibration, and isotopic variability related to sample topography. (*A*) Secondary electron image shows sample texture and topography. (*B*) ^{15}N-enrichment image shows the ^{15}N-abundance on the unlabeled cell. The even isotope ratio across the image demonstrates the ^{15}N-enrichment detected at each pixel is not affected by topography. (*C*) ^{13}C-enrichment image shows the ^{13}C-abundance on the cell. Similar to the ^{13}C-enrichment images acquired from metabolically labeled cells, the speckling in the image is due to low ion counts. The even ^{13}C-enrichment demonstrates that topography does not cause variations in the isotope ratio. These data confirm that ratioing the lipid-specific ion signal at each pixel to the naturally abundant ion eliminates any perceptible signal variations induced by sample topography. Consequently, the regions of high ^{15}N-enrichment observed in the metabolically labeled cells cannot be caused by cell topology.

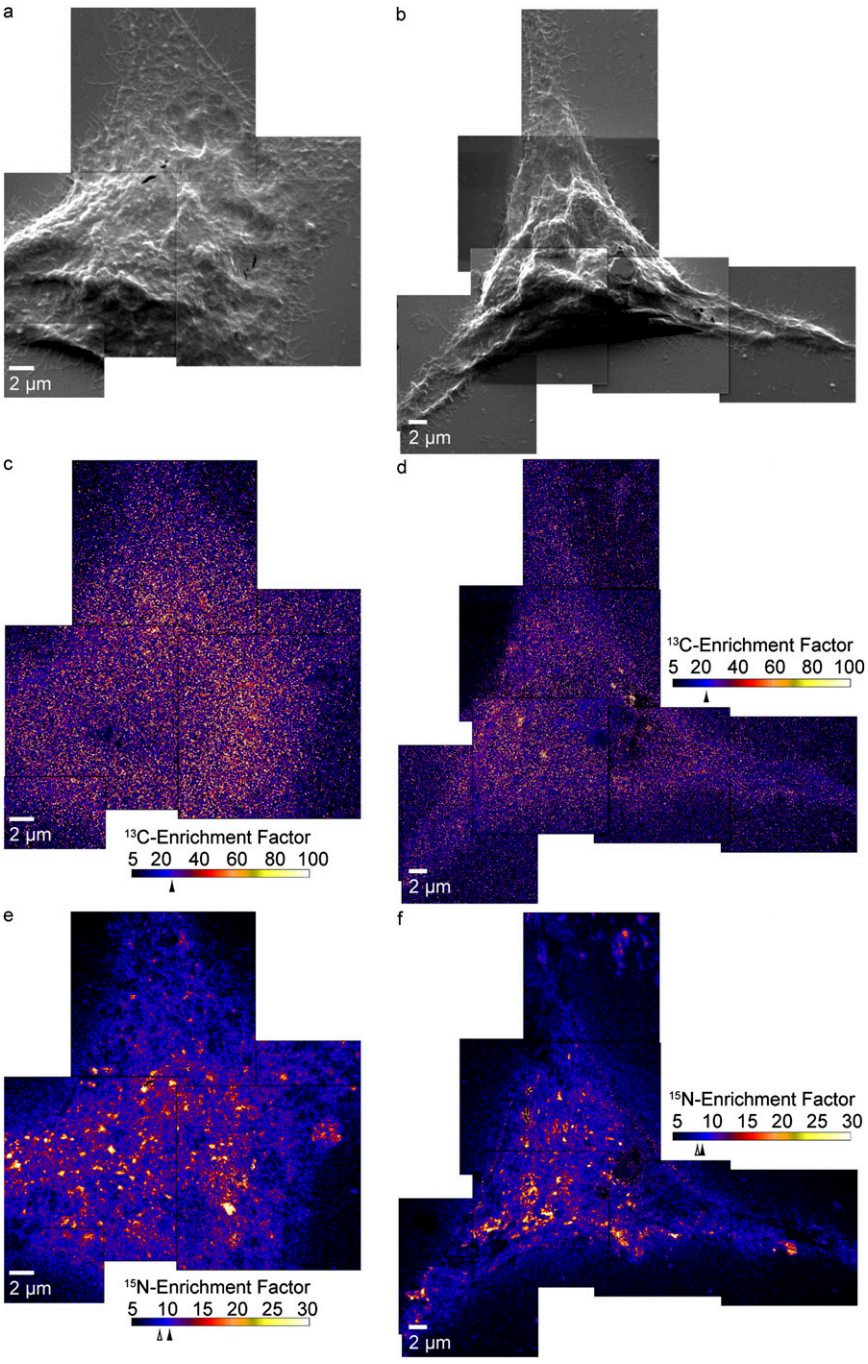

Fig. S3. (*A* and *B*) Montages of 15 × 15-µm secondary electron images of Clone 15 fibroblast cell 2 (*A*) and cell 3 (*B*) were acquired in parallel to the lipid-specific secondary ions. (*C* and *D*) The ^{13}C-enrichment images show the abundance of all ^{13}C-lipid species in the membranes of cell 2 (*C*) and Cell 3 (*D*). Color scales are the $^{13}C^{1}H^{-}/^{12}C^{1}H^{-}$ ratio divided by the natural abundance ratio. Speckling is due to low counts of CH isotopologues. Mean ^{13}C-enrichments on cell 2 and cell 3 (solid arrowhead) are 26.3 (*C*, SD = 23.9) and 22.9 (*D*, SD = 25.6), respectively. (*E* and *F*) The ^{15}N-enrichment images show the abundance of ^{15}N-sphingolipids in the membranes of cell 2 (*E*) and cell 3 (*F*). Color scales show the $^{12}C^{15}N^{-}/^{12}C^{14}N^{-}$ ratio divided by the natural abundance ratio. (*E*) Mean ^{15}N-enrichment factors for the domain-free areas (open arrowhead) and the entire surface (solid arrowhead) of cell 2 are 8.9 (SD = 2.7), and 10.3 (SD = 3.7), respectively. (*F*) The mean ^{15}N-enrichment factors at the domain-free areas (open arrowhead) and the entire surface (solid arrowhead) of cell 3 are 8.4 (SD = 2.7), and 9.1 (SD = 3.7), respectively. This describes C and D, and was moved to the appropriate location in the caption.

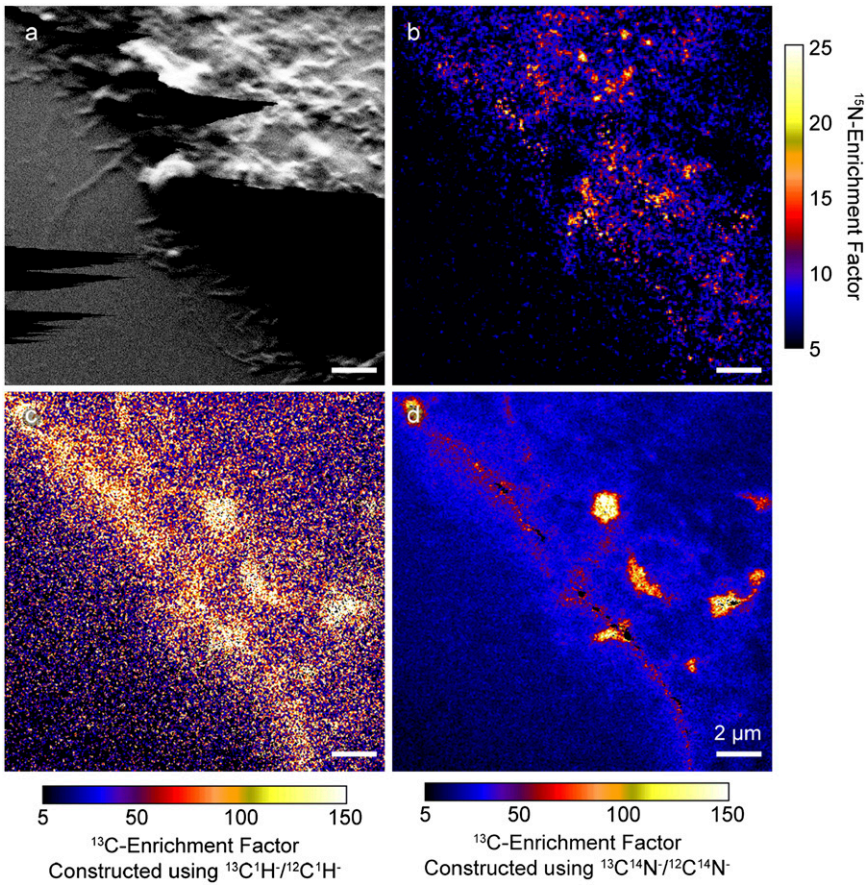

Fig. S4. Comparison of ^{13}C-enrichment measured for a metabolically labeled cell membrane using CH^- and CN^- ions to test for iridium-coating artifacts. (*A*) Secondary electron images of iridium-coated samples show the texture of the cell and adjacent substrate. Secondary electron yields were low at the locations in the image that appear black because of moderate charging with the low primary ion beam current used for imaging. (*B*) ^{15}N-enrichment image of the same location. (*C*) The ^{13}C-enrichment image of the same location was constructed using the ratio of the $^{13}C^1H^-$ to $^{12}C^1H^-$ counts detected at each pixel. (*D*) The ^{13}C-enrichment image was constructed using the ratio of the $^{13}C^{14}N^-$ to $^{12}C^{14}N^-$ counts detected at each pixel. The pattern of isotope enrichment shown in the ^{13}C-enrichment image constructed using the $^{13}C^{14}N^-/^{12}C^{14}N^-$ ratio (*D*) was very similar to the distribution of isotope enrichment shown in the ^{13}C-enrichment image constructed using the $^{13}C^1H^-/^{12}C^1H^-$ ratio (*C*) and did not reflect the pattern of ^{15}N-enrichment shown in *B*. This confirms that potential nitrogen-containing contamination in the iridium coating did not cause the ^{15}N-enrichment to vary significantly as a function of potential variations in the iridium coating thickness.

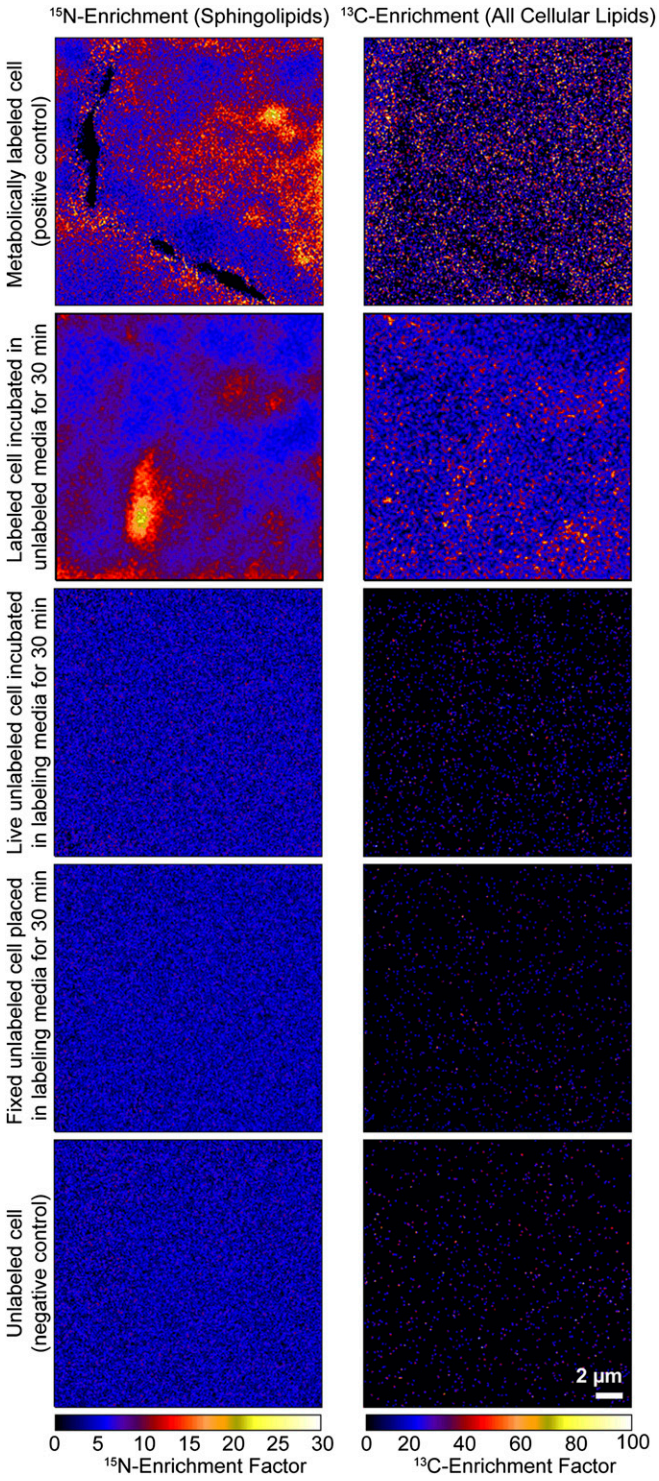

Fig. S5. ^{15}N-enrichment and ^{13}C-enrichment images of Clone 15 fibroblast cell membranes exposed to metabolic labeling medium for various time intervals to test for nonspecific adsorption of labeled material on the cell surface. ^{15}N-enriched domains were present on both the metabolically labeled cell (positive control) and the metabolically labeled cell incubated in label-free (natural abundance) medium for 30 min while alive. The ^{13}C-enrichment images also appear similar. In contrast, the unlabeled cells that were either living or chemically fixed when exposed to labeling medium for 30 min did not exhibit ^{15}N-enriched domains. A low level of ^{13}C-enrichment was observed, suggesting that small amounts of ^{13}C-fatty acids had adhered to the cell or incorporated into the cell membrane. These results indicate that the ^{15}N-enriched domains on the experimental cells were caused by ^{15}N-sphingolipid–enriched domains and not from the adhesion of isotopically labeled material to the surface of the cell.

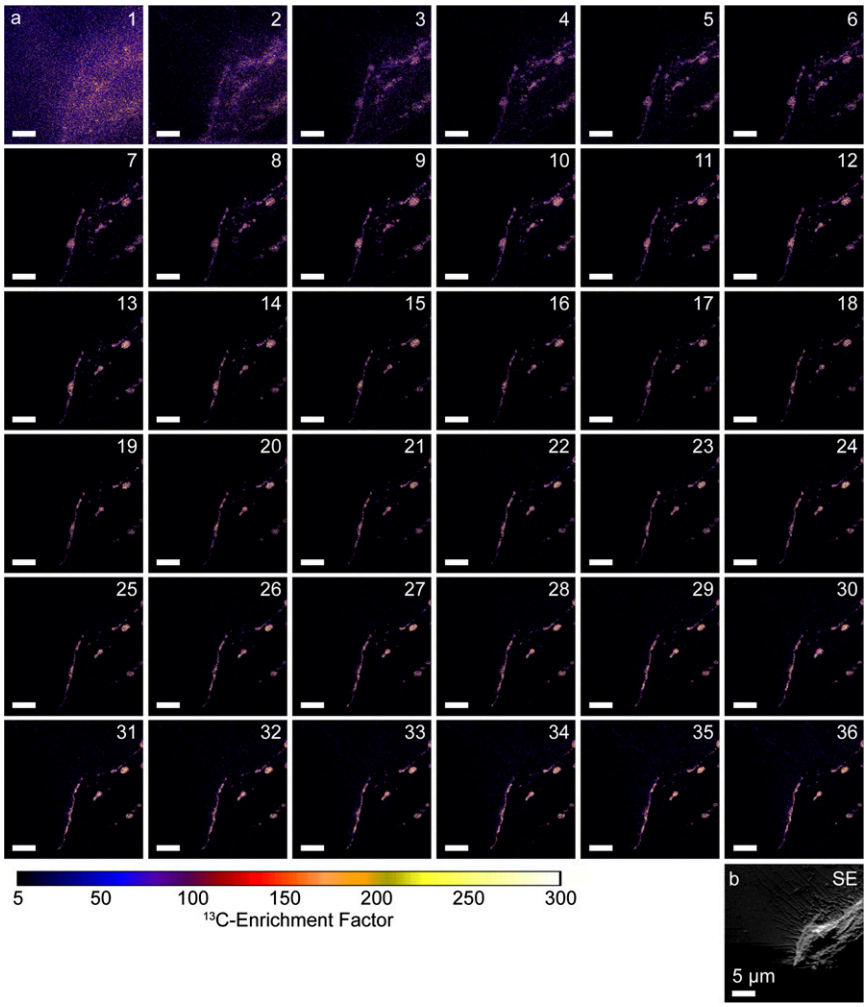

Fig. S6. Three-dimensional distribution of ^{13}C-enrichment in the cell shows elevated ^{13}C-enrichment is specific to cellular membranes. (*A*) A series of 36 NanoSIMS ^{13}C-enrichment images were sequentially acquired at the same sample position on a representative Clone 15 cell that was metabolically labeled and prepared for analysis identically to the cells shown in Fig. S3. To permit analysis of the cytoplasm, the NanoSIMS operating conditions used to acquire these images and those in Figs. S4 and S7 were adjusted so that the sampling depth was approximately four times greater than that used to acquire the rest of the NanoSIMS images presented herein. Approximately 1.3 nm of material was sputtered from the sample surface each time an image was acquired. The elevated ^{13}C-enrichment was continuous at the cell surface, but became discontinuous upon the detection of significant amounts of material within the cytoplasm. Once most of the plasma membrane had been removed (approximately image 6), the ^{13}C-enrichment was elevated only at localized regions within the cytoplasm that likely correspond to organelle membranes and lipid-containing organelles. This confirms that elevated ^{13}C-enrichment is characteristic of cellular membranes. In addition, inspection of the ^{13}C-lipid structures in the cytoplasm shows that their edges remain sharp as the analysis depth increases, which demonstrates that NanoSIMS analysis did not induce biomolecule mixing or alter the lateral distribution of lipids in the sample. Similar results were obtained by depth-profiling measurements made on the four other cells we analyzed. (*B*) The morphology of the cell is shown in the NanoSIMS secondary electron (SE) image of this location. SEs were not detected at the lower portion of the image, likely because secondary electron production is low when the low primary ion beam currents are used for imaging.

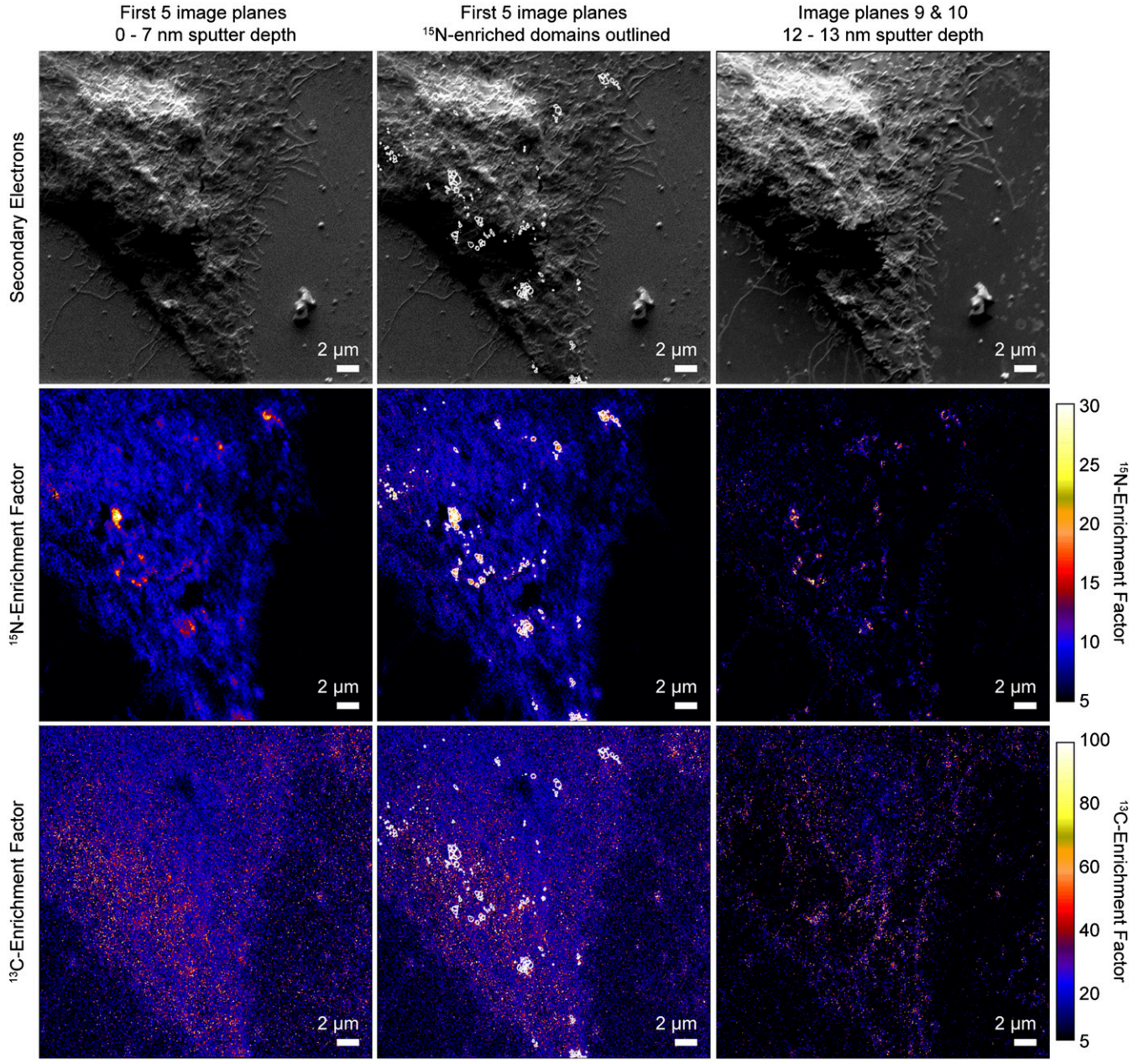

Fig. S7. Elevations in ^{13}C-enrichment at the ^{15}N-enriched domains signify the detection of intracellular membranes. The same location on a metabolically labeled cell was repeatedly analyzed while using a primary ion beam current that was approximately four times higher than that used for the rest of the NanoSIMS analyses presented herein to enable the detection of intracellular membranes and the underlying cytoplasm. The secondary electron, ^{15}N-enrichment, and ^{13}C-enrichment images shown in the *Left* column were constructed from the first five image planes that were sequentially acquired at the same location on the metabolically labeled Clone 15 cell; the sputtering depth was ~7 nm. In the *Center* column, white outlines that locate statistically significant ^{15}N-enriched domains were overlaid on the NanoSIMS images shown in the *Left* column. The ^{15}N-enriched domains exhibited a statistically significant elevation in the local ^{13}C-enrichment (Kolmogrov–Smirnov test, $h = 1$, $P < 10^{-32}$). The elevated ^{15}N- and ^{13}C-enrichments detected at these sites after ~12–13 nm of material was removed from the sample (*Right* column) confirm the presence of intracellular membranes at these sites. Thus, ^{15}N-enriched domains caused by the detection of intracellular membranes exhibit a coelevation in ^{13}C-enrichment that is characteristic of the excess of ^{13}C-lipids present at these sites.

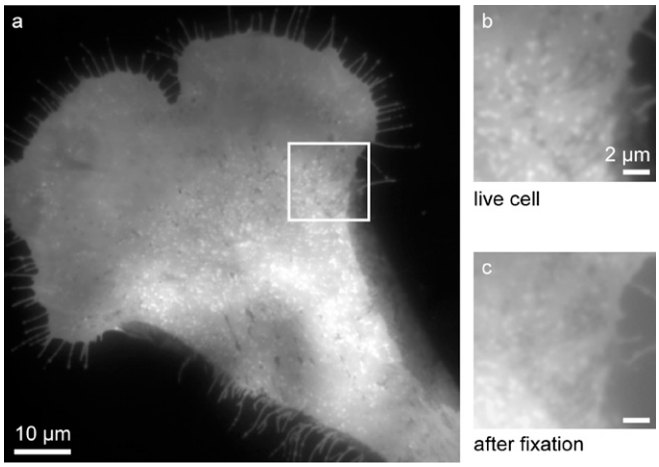

Fig. S8. (*A*–*C*) TIRFM images of borondipyrromethene (BODIPY)-sphingolipid distribution on a Clone 15 cell. Stacks of 120 frames were acquired. Images are those shown in Fig. 4 without background correction. Highly fluorescent patches of BODIPY-sphingolipid domains are visible in the plasma membrane. The enlargement of the outlined region (*B* and *C*) more clearly shows the sizes and shapes of the BODIPY-sphingolipid domains in the plasma membrane. The fluorescence intensities of the cellular microextensions are similar to those of the nondomain regions on the cell body and are much lower than the intensities of the domains on the cell body. This demonstrates that the high fluorescence on the cellular microextensions visible in Fig. 4 is an artifact of background correction and does not indicate that the cellular microextensions are enriched with BODIPY-sphingolipids.

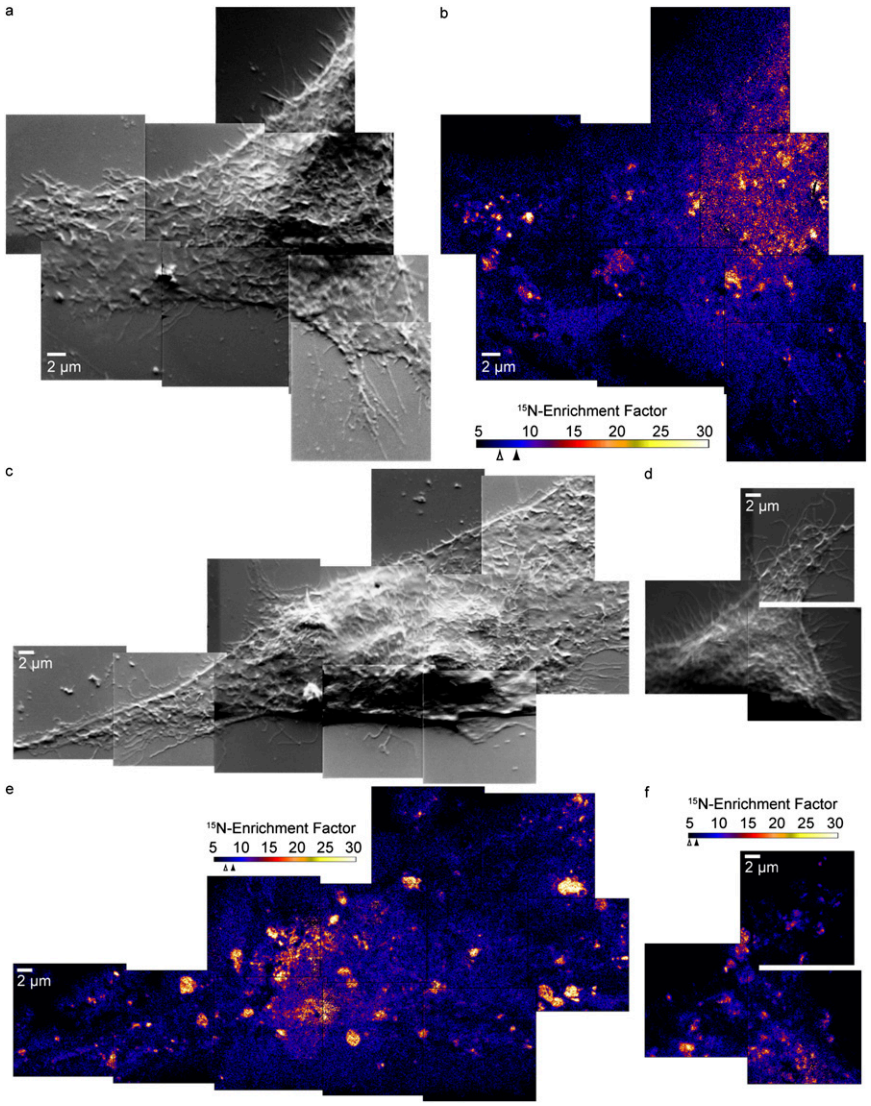

Fig. S9. NanoSIMS images of three additional Clone 15 cells that were fixed with glutaraldehyde at 37 °C. The montages of secondary electron images show Clone 15 cell 1 at 37 °C (*A*), cell 2 at 37 °C (*C*), and cell 3 at 37 °C (*D*) have normal morphology. The ^{15}N-enrichment images show the ^{15}N-sphingolipid abundance in the membranes of Clone 15 cell 1 at 37 °C (*B*), cell 2 at 37 °C (*E*), and cell 3 at 37 °C (*F*). Color scale is the $^{12}C^{15}N^{-}/^{12}C^{14}N^{-}$ ratio divided by the natural abundance ratio. For cell 1 at 37 °C, the mean ^{15}N-enrichment factors for the entire surface and the domain-free regions on the cell are 9.2 (solid arrowhead, SD = 4.8) and 7.4 (open arrowhead, SD = 2.8), respectively. For cell 2 at 37 °C, the mean ^{15}N-enrichment factors for the entire surface (solid arrowhead) and domain-free areas (open arrowhead) are 8.5 (SD = 4.6) and 5.1 (SD = 1.9), respectively. For cell 3 at 37 °C, the mean ^{15}N-enrichment factors for the entire surface (solid arrowhead) and domain-free areas (open arrowhead) are 6.3 (SD = 3.4) and 5.6 (SD = 2.4), respectively.

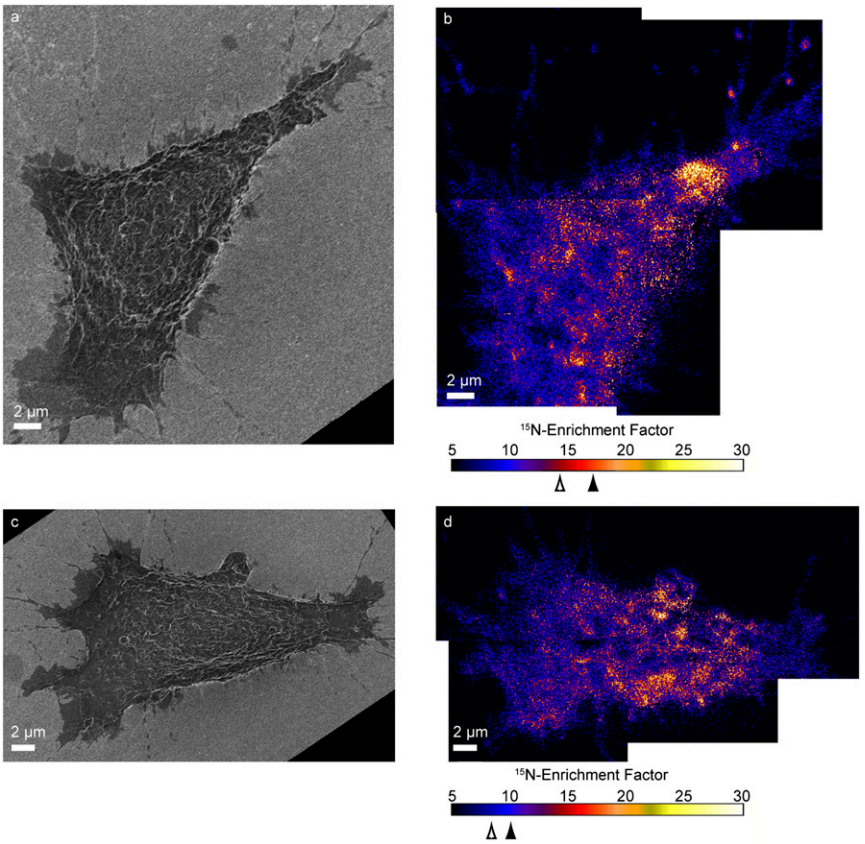

Fig. S10. Secondary electron microscopy (SEM) and NanoSIMS images of additional Clone 15 fibroblast cells that were treated with methyl-β-cyclodextrin (mβCD). (*A* and *C*) SEM images of the second (*A*) and third (*C*) mβCD-treated Clone 15 fibroblast cells (cell 2 mβCD and cell 3 mβCD, respectively) were cropped and rotated for comparison with the NanoSIMS images of the same cells. (*B* and *D*) Montages of ^{15}N-enrichment images of cell 2 mβCD (*B*) and cell 3 mβCD (*D*). The color scale shows the measured ^{15}N-sphingolipid enrichment at each pixel. For cell 2 mβCD, the mean ^{15}N-enrichments for domain-free regions and the entire cell are 14.2 (open arrowhead, SD = 6.9) and 17.2 (solid arrowhead, SD = 11.8), respectively. For cell 3 mβCD, the mean ^{15}N-enrichment factors for domain-free regions and the entire cell are 8.3 (open arrowhead, SD = 3.6), and 10.0 (solid arrowhead, SD = 5.3), respectively.

Table S1. Characteristics of cell membrane area and sphingolipid domains in Clone 15 cells

	Cell 1 RT	Cell 2 RT	Cell 3 RT	Cell 1 37 °C	Cell 2 37 °C	Cell 3 37 °C	Cell 1 mβCD	Cell 2 mβCD	Cell 3 mβCD
Cell surface area, μm^2	718	518	513	1,430	668	357	348	214	237
No. domains	2,190	2,729	1,236	2,352	2,508	1,479	158	342	309
Mean domain area, μm^2	0.033 ± 0.023	0.029 ± 0.026	0.038 ± 0.032	0.033 ± 0.027	0.025 ± 0.020	0.031 ± 0.023	0.025 ± 0.019	0.027 ± 0.019	0.031 ± 0.024
Mean effective domain diameter, nm	194 ± 63	182 ± 67	205 ± 80	194 ± 72	170 ± 58	189 ± 64	170 ± 57	177 ± 59	188 ± 66
Cell surface coverage, %	10	15	9	8	10	13	1	4	4
Domains/μm^2 body	5.8	6.4	3.2	2.7	4.9	5.1	0.9	1.8	1.8
Domains/μm^2 extensions	0.9	1.3	1.1	1.3	0.7	1.4	0.2	0.8	0.5

RT, room temperature.

Table S2. Characteristics of sphingolipid domains on Clone 15 cells that were subjected to various treatments

	Cell 1 RT	Cell 2 RT	Cell 3 RT	Cell 1 37 °C	Cell 2 37 °C	Cell 3 37 °C	Cell 1 mβCD	Cell 2 mβCD	Cell 3 mβCD
Mean ^{15}N-enrichment factor on entire cell, mean ± 1 SD	9.5 ± 3.6	10.3 ± 3.7	9.1 ± 3.7	8.5 ± 4.6	9.2 ± 4.8	6.3 ± 3.4	10.3 ± 8.7	17.2 ± 11.8	10.0 ± 5.3
No. (total area, μm^2) ROIs on cell surface	59,301 (457.5)	65,633 (506.3)	66,655 (514.2)	145,332 (1100)	94,000 (711.5)	130,537 (332.6)	46,232 (349.9)	23,710 (179.1)	28.677 (217.1)
Minimum statistically significant local elevation in ^{15}N-enrichment	12.0	14.3	13.8	8.9	13.0	10.4	21.7	28.0	15.5
Mean ^{15}N-enrichment factor for nondomains	7.8 ± 2.1	8.9 ± 2.7	8.4 ± 2.7	5.1 ± 1.9	7.4 ± 2.8	5.6 ± 2.4	8.9 ± 6.4	14.2 ± 6.9	8.3 ± 3.6
P value for Kolmogrov–Smirnov test of ^{13}C-enrichment factors in domain and nondomain areas ($P < 0.05$ indicates a statistically significant difference)	0.60	0.34	0.59	0.52	0.46	0.50	0.45	0.48	0.49

ROI, region of interest.